Biol. Cell (2008) **100**, 413–425 (Printed in Great Britain) doi:10.1042/BC20070149

Research article

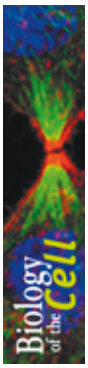

Apo-Hsp90 coexists in two open conformational states in solution

Patrick Bron*, Emmanuel Giudice*, Jean-Paul Rolland*, Rubén M. Bueyt, Pascale Barbier‡, J. Fernando Díaz†, Vincent Peyrot‡, Daniel Thomas* and Cyrille Garnier*[1]

*UMR 6026 Université de Rennes 1 – CNRS, équipe SDM, Campus de Beaulieu, 35042 Rennes, France, †CSIC (Centro de Investigaciones Biologicas), Ramiro de Maeztu 9, 28040 Madrid, Spain, and ‡Inserm-U911, CRO2, Université de la Méditerranée, Faculté de Pharmacie, 27 boulevard Jean Moulin, 13385 Marseille Cedex 5, France

Background information. Hsp90 (90 kDa heat-shock protein) plays a key role in the folding and activation of many client proteins involved in signal transduction and cell cycle control. The cycle of Hsp90 has been intimately associated with large conformational rearrangements, which are nucleotide-binding-dependent. However, up to now, our understanding of Hsp90 conformational changes derives from structural information, which refers to the crystal states of either recombinant Hsp90 constructs or the prokaryotic homologue HtpG (Hsp90 prokaryotic homologue).

Results and discussion. Here, we present the first nucleotide-free structures of the entire eukaryotic Hsp90 (apo-Hsp90) obtained by small-angle X-ray scattering and single-particle cryo-EM (cryo-electron microscopy). We show that, in solution, apo-Hsp90 is in a conformational equilibrium between two open states that have never been described previously. By comparing our cryo-EM maps with HtpG and known Hsp90 structures, we establish that the structural changes involved in switching between the two Hsp90 apo-forms require large movements of the NTD (N-terminal domain) and MD (middle domain) around two flexible hinge regions.

Conclusions. The present study shows, for the first time, the structure of the entire eukaryotic apo-Hsp90, along with its intrinsic flexibility. Although large structural rearrangements, leading to partial closure of the Hsp90 dimer, were previously attributed to the binding of nucleotides, our results reveal that they are in fact mainly due to the intrinsic flexibility of Hsp90 dimer. Taking into account the preponderant role of the dynamic nature of the structure of Hsp90, we reconsider the Hsp90 ATPase cycle.

Introduction

The 90 kDa chaperone protein [Hsp90 (90 kDa heat-shock protein)] is highly conserved and ubiquitously expressed in most living organisms. Hsp90 is essential for cell survival, as it is required for the folding and regulation of many key proteins involved in signal transduction and cell cycle control (Pearl and Prodromou, 2006). Hence, Hsp90 appears to be a promising target for anticancer strategies (Whitesell and Lindquist, 2005). In eukaryotic cells, two Hsp90 isoforms coexist in the cytoplasm: α and β. They associate as elongated homodimers α–α or β–β of ~169 kDa molecular mass (Garnier et al., 2002). Hsp90 is a flexible protein consisting of three well-conserved structural domains: the NTD (N-terminal domain) involved in nucleotide and inhibitor binding; the MD (middle domain) involved in the binding of both co-chaperones and client proteins; and the CTD (C-terminal domain) implicated in dimerization (Harris et al., 2004; Ali et al., 2006). Several structures of these isolated domains have been resolved (Prodromou et al., 1997; Stebbins et al., 1997; Meyer et al., 2003; Harris et al., 2004). Functionally, Hsp90's cycle seems to be driven by the binding and hydrolysis of ATP molecules through transient dimerization of the NTDs (Csermely et al., 1993;

[1]To whom correspondence should be addressed (email cyrille.garnier@univ-rennes1.fr).

Key words: chaperone, cryo-electron microscopy (cryo-EM), intrinsic flexibility, 90 kDa heat-shock protein (Hsp90), small-angle X-ray scattering (SAXS), structure.

Abbreviations used: CTD, C-terminal domain; EM, electron microscopy; Hsp90, 90 kDa heat-shock protein; HtpG, Hsp90 prokaryotic homologue; MD, middle domain; MSA, multi-statistical alignment; NTD, N-terminal domain; SAXS, small-angle X-ray scattering.

Prodromou et al., 2000; Pearl and Prodromou, 2006). In the case of the prokaryotic analogue HtpG (Hsp90 prokaryotic homologue), nucleotide binding seems to induce large structural modifications of the dimer from an open to a closed state (Shiau et al., 2006), whereas these changes are expected to be much more subtle for eukaryotic Hsp90 (Ali et al., 2006; Richter and Buchner, 2006). This molecular clamp mechanism was initially suggested by CD experiments (Csermely et al., 1993), strengthened by rotary-shadowing EM (electron microscopy) (Maruya et al., 1999) and through the recently published structures of the Hsp90 dimer. Indeed, the first closed state was determined from the atomic structure of the Hsp90–p[NH]ppA (adenosine 5′-[β,γ-imido]-triphosphate)–p23/Sba1 co-chaperone complex (Ali et al., 2006). However, it is worth noting that the crystal was obtained using an Hsp90 molecule devoid of its large flexible loops, assumed to be involved in the molecular flexibility of Hsp90 (Csermely et al., 1998; Buchner, 1999). Other closed conformations were described for Hsp90 in complex with the co-chaperone Cdc37 (cell division cycle 37) and the CDK4 (cyclin-dependent kinase 4) client protein by negative staining EM (Vaughan et al., 2006) and by crystallography for HtpG in complex with ADP or ATP (Shiau et al., 2006). On the other hand, the open state was only resolved for apo-HtpG (Harris et al., 2004; Shiau et al., 2006). According to the available atomic structures, it appears that, in spite of the large conformational rearrangements undergone by the Hsp90 dimers, the structures of the individual domains remain very well preserved. Such a structural conservation indicates that the flexibility of the Hsp90 molecule should result from a displacement of the domains with respect to each other around the two hinge regions located between NTD and MD, and between MD and CTD (Richter and Buchner, 2006). Moreover, the current understanding of Hsp90's cycle seems to highlight the role of the remarkable flexibility of the ATP lid in the ATPase cycle (Richter et al., 2006). All of these crystallographic studies have provided much important information, but in many cases they only represent a snapshot of the system referring to static and/or constrained crystalline structures; thus they do not permit us to correctly apprehend the protein dynamics and to really understand how Hsp90 can shift from an open to a closed structure. An interesting recent study investigated Hsp90 conformational changes in solution (Phillips et al., 2007) and revealed that the binding of small ligands at NTD (inhibitors or co-chaperones) induced conformational changes in the MD and CTD. These results suggest long-range effects due to communication between Hsp90's domains. However, the behaviour of apo-Hsp90 dimer in solution is still unresolved, and consequently the potential role of its flexibility in the cycle of Hsp90 remains unknown.

Here, we report the structural investigation of the native pig brain apo-Hsp90 in solution by SAXS (small-angle X-ray scattering) and EM. Our results highlight the intrinsic flexibility of the full-length eukaryotic apo-Hsp90, allowing us to revisit the ATPase cycle of Hsp90.

Results and discussion

The full-length eukaryotic apo-Hsp90 was purified from pig brain. The well-established purification protocol leads to the apo-Hsp90 protein in its dimeric state (Garnier et al., 2002). Our structural investigations were performed without any co-chaperones or nucleotides.

Structural investigation by SAXS

The scattering profile of the apo-Hsp90 dimer and the corresponding pair distribution function are shown in Figures 1(A) and 1(B) respectively. The value for the radius of gyration (R_g) calculated from the Guinier plot was 54.6 ± 0.2 Å (1 Å=0.1 nm; using S values up to $5.087.10^{-3}$ Å^{-1}). Since this region of the scattering intensity curve is especially sensitive to low degrees of aggregation, we also calculated the R_g using the program GNOM (Svergun, 1992). The resulting R_g value was 58.35 Å, after setting the maximum distance to 195 Å (Figure 1B). The reliability of both values is supported by our cryo-EM results.

Our R_g values are slightly smaller than those previously published (Zhang et al., 2004). However, these authors reported some problems with aggregation, especially in the presence of geldanamycin. We also observed a low degree of aggregation, which affected the lower angle part of the curves. We therefore removed this part for further data processing up to 0.05 Å^{-1}.

Then, a three-dimensional low-resolution envelope for apo-Hsp90 was *ab initio* modelled using both a simulating annealing algorithm, implemented in the

Figure 1 | Structural model of the apo-Hsp90 dimer obtained by SAXS analysis

(**A**) Experimental SAXS profile of the apo-Hsp90 dimer (continuous line) and the best fit of the data generated by DAMMIN after imposing P2 symmetry (discontinuous line, $CHI^2 = 1.34$). (**B**) Pair distribution function (including error bars) of Hsp90, generated by GNOM, using a D_{max} of 195 Å. (**C**) Low-resolution envelope views of the *ab initio* three-dimensional model of the apo-Hsp90 dimeric particle in solution obtained by SAXS analysis. The model was generated with DAMMIN corresponding to the fit in (**A**) after imposing P2 symmetry. (**C**) Scale bar, 25 Å.

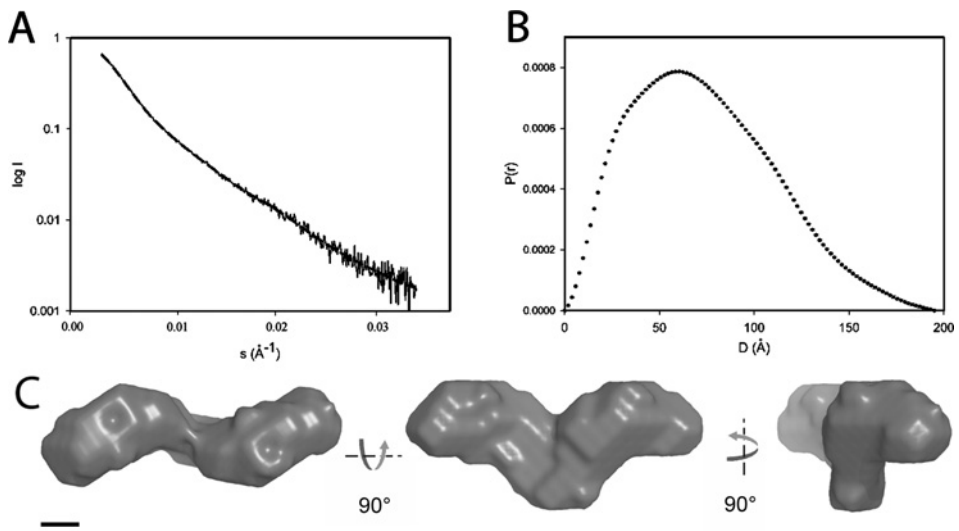

software DAMMIN (Svergun, 1999), and a genetic algorithm, implemented in the software DALAI_GA (Chacon et al., 2000). Figure 1(C) displays the envelope obtained using DAMMIN, and by imposing P2 symmetry restrictions (which best fits the data displayed in Figure 1A). A similar result was generated without imposing symmetry restriction using DALAI_GA (results not shown). It is worth noting that the first Hsp90 envelopes, created without imposing symmetry restrictions during the modelling process, resulted in clearly symmetrical shapes. This prompted us to use P2 symmetry for the next steps of the modelling procedure, using DAMMIN software. The resulting apo-Hsp90 model has an elongated structure with a 'flying seagull' shape ~195 Å long and ~90 Å high, and presents a 2-fold symmetry (Figure 1C). Although computed at low resolution, this three-dimensional model indicates that the protein is structurally quite homogeneous in solution. Furthermore, the presence of the 2-fold symmetry, observed even without imposing symmetry restrictions in the modelling procedure, confirms the dimeric state of apo-Hsp90.

Structural investigation by conventional EM

A structural characterization of apo-Hsp90 by negative staining and rotary-shadowing EM was attempted. Despite trying various stains (uranyl acetate, ammonium molybdate, methylamine vanadate etc.), negative staining yielded poor Hsp90 images. Although the best contrast was obtained with 1% sodium silicotungstate (see Supplementary Figure 1 at http://www.biolcell.org/boc/100/boc1000413add.htm), the molecule still presented a very high degree of conformational variability. In any case, the images acquired using negative staining were unsuitable for image analysis and three-dimensional reconstruction. In contrast to Hsp90, the bacterial homologue HtpG has already been successfully characterized through negative staining and image processing (Shiau et al., 2006), displaying an open 'V' shape with a relatively variable opening angle. However, we can assume that the absence of the charged loop (between NTD and MD) should confer less flexibility and thus less shape variability on HtpG, which may explain why the responses of the two homologous proteins to negative staining are different.

Figure 2 | Metal-shadowed apo-Hsp90 images

Most of the particles present an extended shape (black square), whereas other less numerous particles display a tightly packed shape (arrowheads). TMV (tobacco mosaic virus) was used as an internal standard. Scale bar, 50 nm.

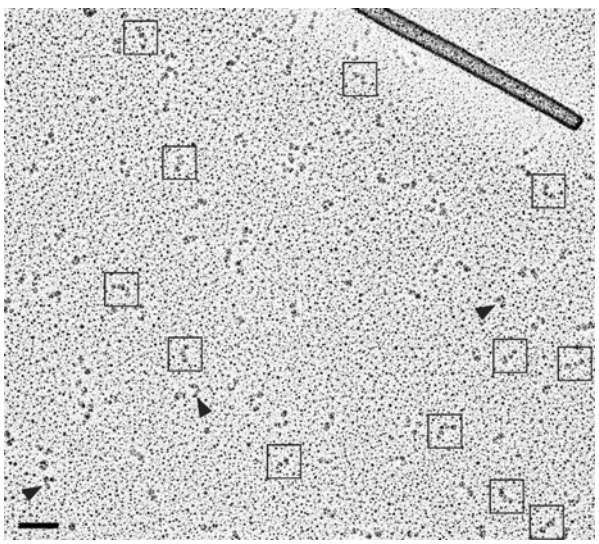

Electron images of Hsp90 dimers were previously published by Maruya et al. (1999), using a low-angle rotary-shadowing EM replica method. Our Hsp90 sample subjected to the same EM preparation gave satisfactory results, as illustrated in Figure 2. Most of the particles have an extended shape (boxes), whereas other less numerous particles display a more tightly packed shape (arrowheads). The particles with the extended shape could be easily related to the 'flying seagull' projection of the SAXS three-dimensional model and to previous EM studies (Koyasu et al., 1986; Maruya et al., 1999). However, the presence of compacted particles suggests that the apo-Hsp90 molecule can adopt other conformational states. Together, SAXS and rotary-shadowing EM data indicate that, in solution, apo-Hsp90 adopts mostly a stretched conformation ('flying seagull'), which is in accordance with the structure of the apo-Hsp90 bacterial homologue HtpG (Shiau et al., 2006). Nevertheless, as we had observed by negative staining, rotary-shadowing EM images also show that apo-Hsp90, in the absence of ligand (nucleotide, inhibitors or co-chaperone), presents a high flexibility.

Structural investigation by cryo-EM: three-dimensional reconstructions and map comparison of the two open states

Cryo-EM has established itself as a valuable method for the structural determination of protein molecules. Combined with single-particle analysis and averaging, a three-dimensional structure can be calculated. However, this technique has been used mainly with large proteins having molecular masses over 500 kDa. With respect to the molecular mass of the Hsp90 dimer (169 kDa), the first challenge was to record images of frozen-hydrated apo-Hsp90 particles. In most micrographs, apo-Hsp90 particles were blurred or quasi-invisible. However, when the ice was extremely thin, it was sometimes possible to distinguish particles (see Supplementary Figure 2 at http://www.biolcell.org/boc/100/boc1000413add.htm). Although the signal-to-noise ratio was extremely low, the apo-Hsp90 particles could be observed when applying a local low-pass filter. A set of filtered images of apo-Hsp90 particles is shown in Figure 3. Some of these display shapes that are consistent with the apo-Hsp90 structure revealed by SAXS and rotary-shadowing EM, but it is difficult to assign most of the particles to a putative structure. We assumed that although frozen-hydrated apo-Hsp90 particles were quasi-invisible in the raw images, image processing of a large number of images of single particles with elongated shape should sufficiently increase the signal-to-noise ratio, allowing the computation of a reliable three-dimensional reconstruction of apo-Hsp90. More than 600 micrographs were recorded but only six were selected, from which 9030 individual particles of apo-Hsp90 were extracted and analysed using IMAGIC V software (van Heel et al., 1996).

The first step consisted of checking the image analysis feasibility, using the three-dimensional SAXS model as a starting reference. After two iterative cycles of image alignment, a three-dimensional model was computed. As expected, it presents similar structural features to the SAXS reference model. Nevertheless, although performed under borderline conditions, it was found that it is possible to extract structural information about such small proteins from cryo-EM images. The use of the SAXS model as a starting reference may induce a bias; consequently, we engaged in a second step: an image analysis of apo-Hsp90 particles without an *a priori* model.

Figure 3 | A set of individual particle images
Examples of particles extracted from a low-pass-filtered cryo-image. The proteins are seen in white and show very high variability in shape. However, some of them show elongated shape (7, 10, 14 and 17) compatible with the 'flying seagull' conformation, whereas other less numerous ones (12 and 24) display a more compacted conformation. The size of the box is 27.7 nm × 27.7 nm.

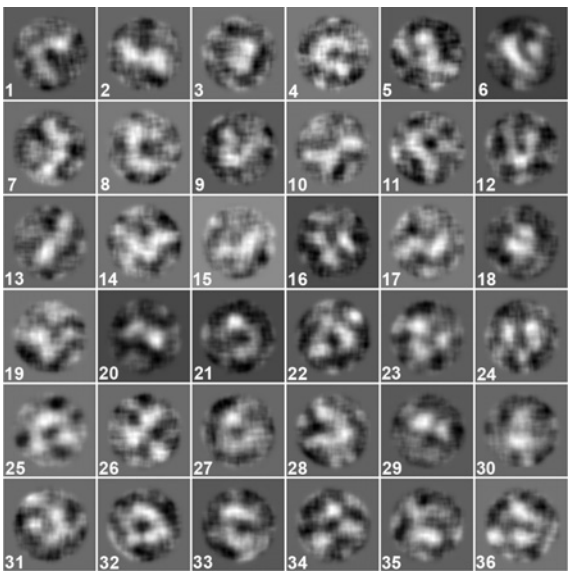

The main problem was to compute reliable class averages by centring and aligning extremely low-contrast particles. The raw images were low-pass-filtered and examined individually. The particles were selected on the basis of their contrast, and their well-defined shape. Our images analysis without an *a priori* model comprised three rounds.

For the first round, 900 references were manually selected. They presented a high degree of shape variability, as shown in Figure 3. These references were used to align all raw images, which were then grouped into classes and averaged. The class averages presenting a high signal-to-noise ratio and a well-characterized shape were extracted to serve as new references.

In the second round, these new references were used for the complete alignment and averaging of all 9030 raw images. Some of the images in the new class averages displayed highly elongated shapes, very similar to those observed when using the SAXS model as a starting reference. Therefore we started the three-dimensional angular reconstruction procedure by using three typical views of the particle with a 'flying seagull' shape. Amazingly, some class averages presented a very high angular error factor; they were temporally excluded in the reconstructed three-dimensional model. A close inspection of them clearly indicated that they referred to a different three-dimensional structure with a 'V' shape. This was not surprising considering the shape of some particles observed using rotary-shadowing EM. Thus we decided to separately analyse all these divergent class averages. Three typical views of particle with a 'V' shape were selected, in order to start the procedure of three-dimensional angular reconstruction. Consequently, two three-dimensional models, one related to the 'flying seagull' and the other to a 'V'-like shape, were reconstructed from the class averages.

In the third round, we applied an iterative procedure to optimize both of the three-dimensional models. A total of 100–150 two-dimensional projections were computed from each three-dimensional model and used as a new set of references to align and average all of the 9030 raw images into new class averages. Then, with respect to the two initial three-dimensional models, Euler angles were attributed to these new class averages. Two new three-dimensional models were reconstructed and refined by comparing their two-dimensional projections with the corresponding class averages. The projections of the two three-dimensional models were then used to improve the alignment of the apo-Hsp90 particle images. This procedure was iteratively applied until the three-dimensional models became stable. After the second iteration, C2 symmetry was imposed on the three-dimensional reconstructions. The use of C2 symmetry was supported by the facts that, in solution, apo-Hsp90 is a dimer and that the SAXS model presents a 2-fold symmetry. Despite the extremely low signal-to-noise ratio, two-thirds of the 9030 originally selected images of apo-Hsp90 particles were assigned to two-dimensional projections of one of the three-dimensional models.

In conclusion, the image analysis that we performed without an *a priori* model allowed us to identify two molecular structures of apo-Hsp90. The first one, which corresponds to 90% of the particle's population, was named the 'fully-open' state. Its three-dimensional EM reconstruction, computed at 28 Å resolution, is shown in Figure 4(A). It has an elongated 'flying seagull' shape structure ~190 Å

Figure 4 | Three-dimensional reconstructions of the native eukaryotic apo-Hsp90 obtained by single-particle cryo-EM analysis and map comparison

(**A**) Different views of the predominant state. A total of 5587 images were included in the final three-dimensional map. The model was built with C2 symmetry. The rectangular shape at the base of the three-dimensional volume is shown (dotted rectangle). (**i**) Representative class averages of the fully-open apo-Hsp90. (**ii**) Reprojections of the fully open three-dimensional structure of apo-Hsp90 in the orientations found for the class averages in (**i**). (**B**) Same as (**A**), but showing the minority state of apo-Hsp90. A total of 598 images were included in the final EM map. The size of individual class averages and reprojections is 33.5 nm × 33.5 nm. (**C**) (**i**, **ii**) Specific views of the two EM maps highlighting the singular triangular shape and especially the flat side of the hands (broken lines). The mobile region, corresponding to the MD and NTD of one of the monomers, is shown in yellow and blue for the fully-open and semi-open maps respectively. (**iii**) Two views of the superimposition of the cryo-EM maps showing the structural rearrangements required to shift from the fully-open to the semi-open state. Scale bars, 25 Å.

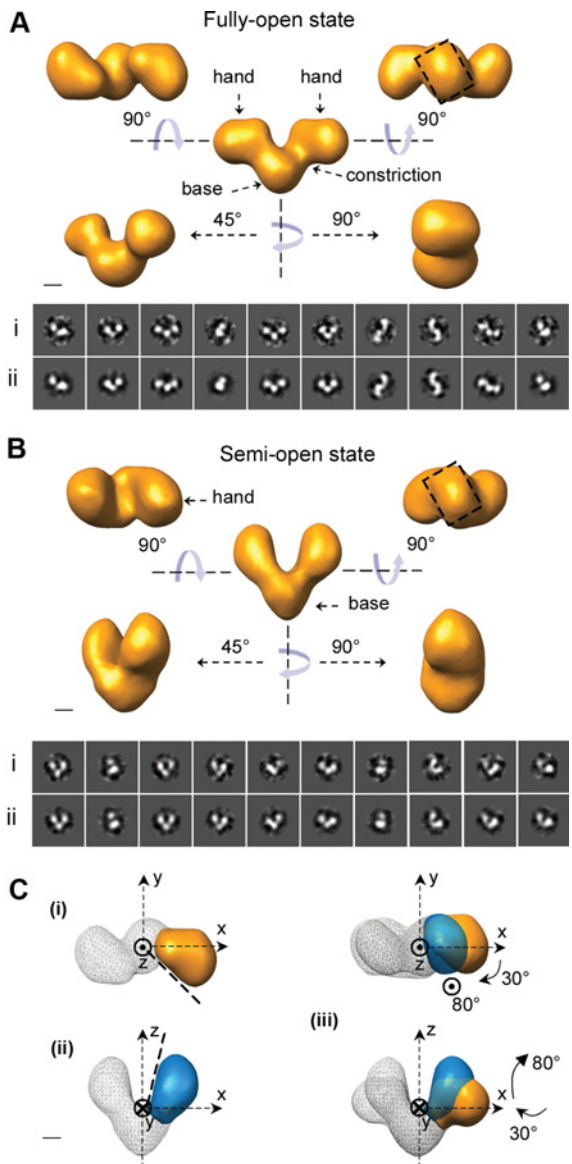

long, with broken wings in which extremities point in opposite directions. Broken wing extremities, or 'hands', display a singular feature formed by a triangular domain with a pronounced flat side. Hands are connected to the basal domain by a constriction of ~40 Å in diameter, and the basal domain has a rectangular shape. The second structure, corresponding to the remaining 10% of the particle's population, was called the 'semi-open' state. Its three-dimensional EM reconstruction, computed at 40 Å resolution, is presented in Figure 4(B). The two hands are closer to the symmetry axis than in the fully-open state, they point in the same direction, and the constrictions are less pronounced. For each monomer, the basal domain, constriction and hand are located along one axis, resulting in a true 'V' dimeric structure. The basal domain displays the same rectangular shape as the fully-open state and the two domains are superimposable. The structural features of the hands are less distinct; nevertheless, we can once more recognize the triangular domain, and especially its flat side. These two cryo-EM maps are the first resolved structures of the full-length eukaryotic apo-Hsp90 in solution. They reveal that the apo-Hsp90 molecule coexists in two open states. These two states reflect a conformational equilibrium in solution attributable to an intrinsic flexibility of the apo-Hsp90 dimer molecule. Considering previous biochemical and structural studies and the presence of a 2-fold axis symmetry obtained for both states, the basal domain unambiguously corresponds to the dimerization domains, i.e. the interaction of the two CTDs. Consequently, the constrictions and hands correspond to the MDs and NTDs respectively.

Hsp90 flexibility revealed by comparison of cryo-EM maps

To understand apo-Hsp90 intrinsic flexibility, the two cryo-EM maps were compared (Figure 4C).

The structural modifications required to switch from the fully-open to the semi-open state are not straightforward. In order to see the singular triangular shape of both fully-open and semi-open hands presenting their flat sides, the cryo-EM maps must be observed in two different specific quasi-orthogonal views (Figures 4Ci and 4Cii). These unique structural features should be conserved even through conformational changes. Because of its conserved rectangular shape, the basal domain was used as the reference to align the two cryo-EM maps (Figure 4Ciii). Comparison of the two superposed maps reveals that to bring the fully-open state hands on the semi-open ones, one must combine two separate rotations: ~30° in the (*x*,*y*)-plane and then ~80° in the (*y*,*z*)-plane. Thus, starting from the fully-open state, the hands of both monomers describe a clockwise movement around the dimer's symmetry axis (z) to reach the semi-open state.

Agreement between SAXS and cryo-EM

Both SAXS and cryo-EM enable the study of the structural organization of the apo-Hsp90 dimer in aqueous solution. Two different *ab initio* three-dimensional reconstruction algorithms were used to construct a low-resolution model that matches the SAXS experimental data. Independently, a three-dimensional reconstruction was obtained from cryo-EM data. Both approaches have converging results: an elongated 'flying seagull'-shaped molecule of ~190 Å length with broken wings. Nevertheless, the two reconstructions present two significant structural differences (Figure 5). First, the CTDs appear to have a much smaller volume in the SAXS model than in the cryo-EM map. Secondly, the SAXS model presents elongated NTDs, whereas in cryo-EM, the fully-open map displays a singular feature formed by a triangular domain with a pronounced flat side. Moreover, in SAXS, only the major open structure of apo-Hsp90 was identified. Indeed, Hsp90 flexibility leads to a high variability in the molecule's shape. However, owing to the random orientation of the solvated molecules, a spatial averaging occurs in SAXS leading to a loss of information. Deconvolution of the SAXS spectra would be possible if enough contribution from the minor conformer is present (Andreu et al., 1994; Diaz et al., 1996) but not with the small contribution expected from the V-shaped (10%). Nevertheless, the SAXS model serves as an illustration that the experimental data can be consistent with an actual physical particle, and it validates our cryo-EM results by elucidating some general features of the average Hsp90 population. On the other hand, the statistical analysis of cryo-EM images overcomes the problem of shape polydispersity, as this technique segregates the molecules into classes. These classes are then averaged, resulting in a more stable picture of the molecule, with low variance and a more finely detailed structure. SAXS models can be very helpful for cryo-EM structural studies of small molecules, such as Hsp90, although such an investigation should be used carefully. In the present study, both SAXS and cryo-EM allowed us to identify the major structural state of apo-Hsp90, whereas the minor semi-open state was only revealed by cryo-EM followed by single-particle analysis performed without an *a priori* model.

Figure 5 | Superimposition of the SAXS model with the apo-Hsp90 fully-open EM map

SAXS (blue) and EM (red) approaches converge to the similar elongated 'flying seagull'-shaped molecule of ~190 Å length with broken wings. Nevertheless, the two reconstructions present significant structural differences: the CTDs appear to have a much smaller volume in the SAXS model than in the cryo-EM map; the SAXS model presents elongated NTDs, whereas in cryo-EM, the fully-open map displays a singular feature formed by a triangular domain with a pronounced flat side. Scale bar, 25 Å.

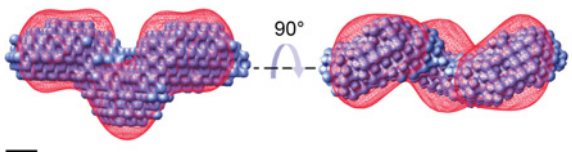

Relationship between EM maps and atomic structures of the Hsp90 dimer

The atomic structure of apo-HtpG published by Shiau and collaborators (Shiau et al., 2006) showed that apo-HtpG adopts an open structure in crystals. In order to determine which of our two cryo-EM maps could correspond to the apo-HtpG open structure, we compared our maps with the apo-HtpG atomic structure (Figure 6). The apo-HtpG structure was placed into the cryo-EM maps by positioning its CTDs into the basal domain of the apo-Hsp90. The apo-HtpG structure fits well into both cryo-EM maps, leaving

Figure 6 | Comparison of cryo-EM maps of apo-Hsp90 with the apo-HtpG atomic structure

(**A**) Positions of the start and the end of the apo-HtpG charged loop indicated by arrows. (**B**) View of the apo-HtpG structure fitted into the fully-open apo-Hsp90 cryo-EM map. The HtpG unoccupied volumes (named 1 and 2 in the text) are delineated by dotted lines. (**C**) View of the apo-HtpG structure fitted into the semi-open apo-Hsp90 cryo-EM map. The HtpG unoccupied volume (named 3 in the text) is delineated by dotted lines. Compared with (**B**), the dimer has been rotated by 90°.

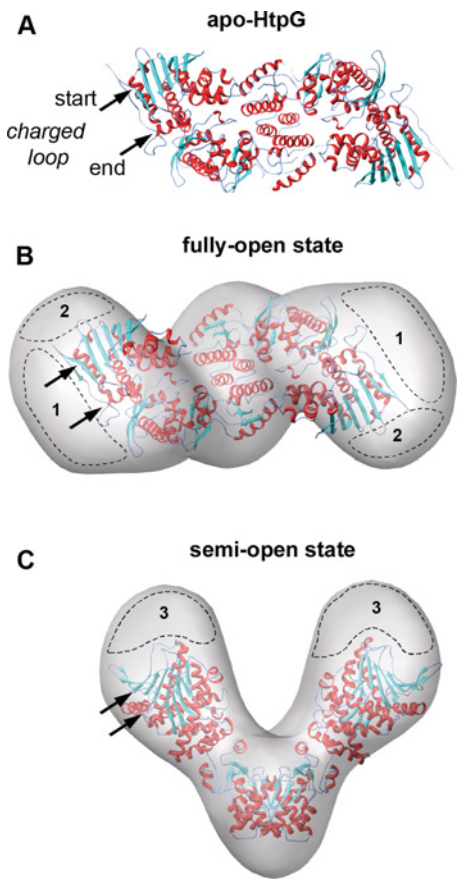

only two small, unoccupied volumes in the fully-open apo-Hsp90 cryo-EM map (Figure 6B, '1' and '2'), and one in the semi-open map (Figure 6C, 3). At this stage, it is worth noting that eukaryotic Hsp90 has a larger charged loop (amino acids 200–280) than in the homologous apo-HtpG (amino acids 227–233). This loop, which represents 11% of the monomer volume, must strongly contribute to the density in the cryo-EM maps. Thus, after the superimposition of the apo-HtpG structure on to the two cryo-EM maps, we expected to find an unoccupied volume near the location of the apo-HtpG small charged loop. In Figure 6, arrows indicate the positions of the start and end of the apo-HtpG charged loop in the two possible fits. Additionally, we have delineated all unoccupied volumes in both cryo-EM maps. The location of the loop perfectly coincides with the empty volume noted as volume 1 in the fully-open apo-Hsp90 cryo-EM map. This location of the charged loop is in agreement with the published structural modelling of human Hsp90 (Phillips et al., 2007). On the other hand, the fit of apo-HtpG into the semi-open apo-Hsp90 cryo-EM map shows that the start and end of the charged loop do not correspond to a neighbouring empty volume in the map. The unoccupied volume, denoted by '3' in the semi-open cryo-EM map, is located above the NTDs, making the occupation of this position by the charged loop more unlikely because of the strong internal reorganization it implies. In conclusion, due to the position of the small homologue loop in apo-HtpG, we can unambiguously localize the Hsp90's large charged loop in the unoccupied volume 1 of the fully-open map, revealing that the fully-open state of apo-Hsp90 is related to the apo-HtpG structure. Nevertheless, some HtpG amino acids still protrude from the inner/upper faces of the apo-Hsp90 fully-open map (Figures 6B, 7A and 7B), which indicates that a supplementary opening of apo-HtpG NTDs may be required to fit into the map. In this case, the opening of NTDs would lead to the occupation of the empty volume 2 in the EM map. To summarize, although fully-open apo-Hsp90 corresponds to the apo-HtpG, the superimposition clearly indicates that it is somewhat different, and that apo-Hsp90 adopts a more relaxed conformation when in solution than apo-HtpG does in crystal. The same observation can be made when comparing the fully-open apo-Hsp90 structure with the recently published Hsp90 structural model (Phillips et al., 2007).

In the case of the semi-open apo-Hsp90 cryo-EM map, the empty volume 3 cannot be directly related to the presence of the large charged loop, which suggests that further structural rearrangements are to be considered. In the presence of ATP (Ali et al., 2006) or ADP (Shiau et al., 2006), Hsp90 and HtpG adopt closed conformations, which differ by a twist of the NTDs (Richter and Buchner, 2006), easily shown by the relative position of the NTDs' first β-sheet (grey triangles in Figures 7C and 7D). In this context, as

Figure 7 | Movements required to reach the ATP- or ADP-Hsp90 closed structure from the apo-HtpG atomic structure (**A**, **B**) Views of the fit of apo-HtpG into the apo-Hsp90 fully-open cryo-EM map. One monomer of apo-HtpG is displayed in cartoon mode and the other in surface-representation mode. Black arrows indicate the position of the large charged loop. Unoccupied volumes named 1 and 2 are delineated by dotted lines. (**B**) Structural rearrangements of apo-HtpG required to reach the closed ATP-Hsp90 (**C**) or ADP-Hsp90 (**D**) structure. The clockwise and anticlockwise movements are schematized by orange and green arrows respectively. (**C**, **D**) The light grey and dark grey triangles indicate the relative positions of the first NTDs' β-sheets at the front and back of the (*x*,*z*)-plane respectively.

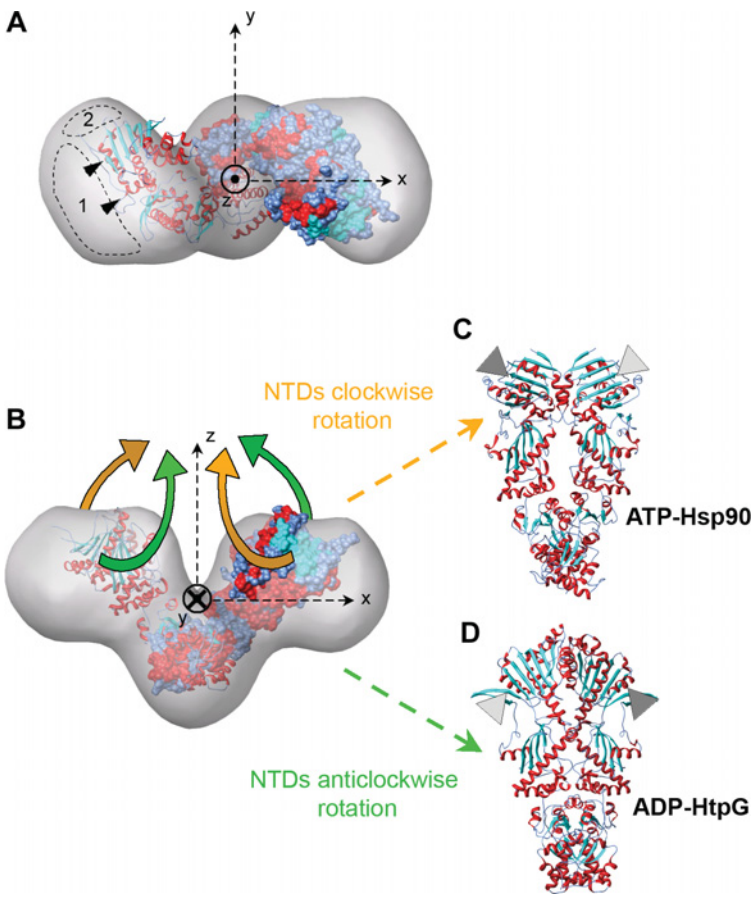

indicated by arrows in Figure 7(B), to switch from the open state of apo-HtpG to the ATP-Hsp90 conformation (Figure 7C), a clockwise rotation of NTDs around the *z*-axis is necessary, whereas an anticlockwise rotation of NTDs is required to converge with the ADP-HtpG conformation (Figure 7D). Nevertheless, the comparison of the two cryo-EM maps permits us to demonstrate that a clockwise movement is required to switch from the fully-open to the semi-open states. This means that the semi-open density map corresponds to an intermediate state between the fully-open state of apo-Hsp90 and the closed state of ATP-Hsp90.

Conclusions

The aim of the present study was to investigate the structure of the entire eukaryotic Hsp90 in the absence of nucleotides. We have demonstrated that apo-Hsp90 is sensitive to stains, excluding structural characterization by negative or cryo-negative staining. However, we showed using SAXS that in solution and without nucleotides, apo-Hsp90 was homogeneous in size and shape and presented a 'flying seagull'-shaped structure. This specific shape was also observed by rotary-shadowing EM experiments. This particular shape and the fact that apo-Hsp90 was homogeneous in solution were good arguments

for attempting the investigation of eukaryotic apo-Hsp90's structure by cryo-EM and image processing. Cryo-EM analysis permitted us to identify two open structural states that have never been described previously, which we named fully-open and semi-open. Although it was at low resolution, our structural approach allowed us to describe these two conformational states and thus to elucidate the dynamic flexibility of the apo-Hsp90 dimer. Moreover, these results demonstrate that it is truly possible to gain structural information by the cryo-EM and image processing of small biological objects having such singular shapes. For the first time, the intrinsic flexibility of Hsp90, which was previously proposed in other studies (Csermely et al., 1998; Buchner, 1999), is now clearly demonstrated for eukaryotic Hsp90. Our comparison of apo-Hsp90 cryo-EM maps with apo-HtpG revealed that, despite some structural differences, the fully-open state is similar to the open structure of apo-HtpG. Moreover, we demonstrate that the amplitude of structural changes between the open and closed conformations is much more pronounced for the eukaryotic Hsp90 than for prokaryotic HtpG. The major structural changes of apo-Hsp90 observed in switching from the fully-open to the semi-open state are the result of clockwise movements of the NTDs around the 2-fold axis symmetry. These large structural rearrangements are intrinsic properties of the apo-Hsp90 dimer and, therefore, are not induced by the binding of nucleotides. Furthermore, the clockwise movements of NTDs described here are opposite to those suggested and occurring during ATP hydrolysis (Richter and Buchner, 2006; Shiau et al., 2006). This natural intrinsic flexibility should be involved in the chaperoning function of the protein, either in the accommodation of structurally numerous co-chaperones and client proteins (Hawle et al., 2006), or in the client protein stabilization, even in the absence of nucleotides (C. Garnier, F. Weis, C. Heichette and D. Chrétien, unpublished data), or in the regulation of nucleotide binding.

In this context, we propose to reconsider Hsp90's cycle, taking into account the preponderant role of the dynamic nature of the Hsp90 dimer (Figure 8). In the first step of the Hsp90 cycle, intrinsic flexibility permits the adaptation of the apo-Hsp90 dimer structure to client proteins, explaining its nucleotide-independent stabilization effect. Moreover, it is clear that, *in vivo*, the presentation of client proteins to

Figure 8 | Hsp90 ATPase cycle related to the intrinsic flexibility of Hsp90

EM structures are schematized in red, whereas atomic structures resolved by X-ray crystallography are in blue. P* and P refer to unfolded and folded client proteins respectively. Grey arrows indicate the domain movements necessary to reach the next state according to the cycle. Orange arrows represent the relative affinity of apo-Hsp90 conformations for nucleotides.

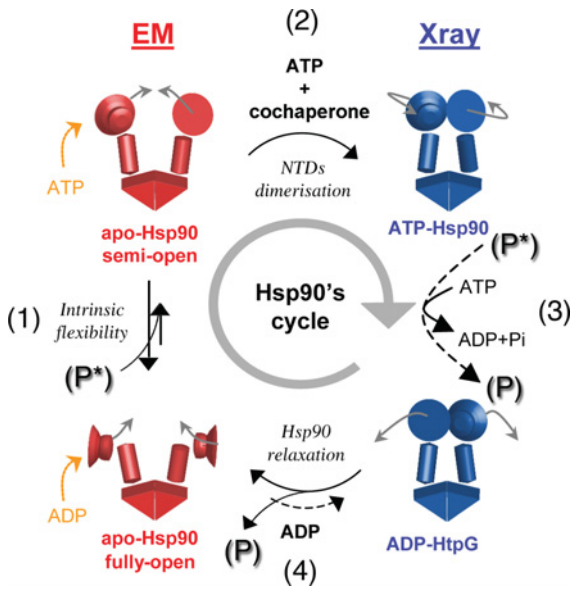

Hsp90 requires a cohort of co-chaperone proteins, including other Hsps (such as Hsp40 and Hsp70), the co-chaperone adaptor Hop, the high-molecular-mass immunophilins and probably many more. Hsp90 seems to be the central protein in the formation of these intermediate complexes; this role implies a high capacity for structural adaptation, made possible by its intrinsic flexibility. The binding of the client protein and co-chaperones progressively displaces the conformational equilibrium towards the semi-open state (clockwise movement), increasing the Hsp90's affinity towards ATP [(1) in Figure 8]. The binding of ATP stabilizes the already formed complex between Hsp90, co-chaperones and its unfolded client protein, while other regulatory co-chaperones (such as p23) help the closure of the Hsp90 dimer [(2) in Figure 8]. A mature Hsp90–ATP–co-chaperone complex would constitute a cellular folding machine. The Hsp90 NTDs' transient dimerization induces the ATP hydrolysis and the NTD rotation,

whereas structural rearrangements of Hsp90 are transmitted on to the bound client protein [(3) in Figure 8]: anticlockwise twist-and-fold movement (Richter and Buchner, 2006). A simple relaxation of the Hsp90 dimer is then sufficient to release both client folded proteins and co-chaperones, restoring the fully-open state [(4) in Figure 8]. The natural intrinsic flexibility of the Hsp90 dimer allows the chaperone protein to prepare for a new ATPase cycle.

Materials and methods

Protein purification

Apo-Hsp90 was purified from pig brains by the method of Yonezawa et al. (1988) modified by Garnier et al. (1998a, 1998b). During purification, proteins were extensively dialysed without any nucleotides. $HClO_4$ precipitation and absorbance measurements of supernatant did not reveal the presence of any nucleotide (C. Garnier, unpublished data). Samples were stored at –80 °C. Protein concentration was determined by measuring UV absorption with a molar absorption coefficient ($\varepsilon_{280\,nm}$) of $124\,000 \pm 6000\ M^{-1} \cdot cm^{-1}$ in 20 mM Tris/HCl buffer (pH 7.5) considering that Hsp90 is a dimer. The absorption was corrected for light scattering using the Beckman DU640B spectrophotometer software. Before analysing, the Hsp90 sample was ultracentrifuged at 50 000 rev./min for 30 min at 4 °C (TLA100 rotor, Beckman TL-100 ultracentrifuge).

SAXS measurements

Data collection was performed at synchrotron Station 2.1 at the Daresbury Laboratory (Daresbury, Warrington, U.K.). Before measuring, the protein concentration was adjusted to 1 or 3 mg/ml and the protein was centrifuged at 55 000 rev./min for 30 min at 4 °C (TLA120.2 rotor, Beckman TLX ultracentrifuge) to pellet possible aggregates. Data were collected at 4 °C using a 200 μl moving cell (5 mm up and down) to minimize sample radiation damage. Two cameras, 6 and 3 m long, were set up to cover the ranges of the scattering vector (defined as reciprocal Bragg spacing, $2\sin\phi/\lambda$) from approx. 0.001 to 0.033 $Å^{-1}$. The absolute values of the scattering vector were measured using the 67 nm repeat in rat's tail wet collagen as a reference. The X-ray scattering profiles were recorded in time frames ranging from 15 to 60 s. Data processing was performed using the software package facilitated by the Collaborative Computational Project for Fibre Diffraction and Solution Scattering (http://www.ccp13.ac.uk/software/software.htm). The data were normalized by beam intensity and detector response before processing. Radiation damage due to the intense X-ray beam was checked, and in cases of damage these time frames were removed before averaging. Radius of gyration and zero intensity of the experimental data curve were calculated using GNOM (Svergun, 1999). Radius of gyration was also calculated from the Guinier plot. Low-resolution structures of the proteins were modelled using programs based on the genetic algorithm DALAI_GA (Chacon et al., 2000) and the simulated annealing algorithm DAMMIN (Svergun, 1999). Fifteen models were generated, and the low-resolution envelope was obtained by superimposing individual runs with the program SUPCOMB (Kozin and Svergun, 2001; Volkov and Svergun, 2003). Given several models from different runs, all possible pairs were aligned to determine the most probable structure and to discard the most divergent models. The model with the lowest average spatial discrepancy was considered to be the most probable, and those with the highest spatial discrepancies were considered as outliers. The included aligned structures were then averaged using DAMAVER and filtered with DAMFILT (Kozin and Svergun, 2001; Volkov and Svergun, 2003), using the average excluded volume as the cut-off.

Rotary-shadowing EM

Apo-Hsp90 at 0.25 mg/ml was mixed with 50% (v/v) glycerol and then sprayed on to a freshly cleaved mica plate. The sample was placed on the rotary stage of a freeze etching device, dried under vacuum and rotary shadowed with platinum at an elevation angle of 5°, followed by carbon evaporation at 90°. The replica was examined with a Philips CM12 electron microscope.

Cryo-EM

The sample was diluted to a final concentration of 15 μM before being applied to Lacey carbon grids. The excess solution was blotted, and the grid was flash-frozen in liquid ethane, resulting in Hsp90 dimers embedded in a thin film of vitrified ice. Electron micrographs were recorded under low-dose conditions at liquid-N_2 temperature with a Tecnai Sphera LaB6 200 kV microscope. Images were collected at × 50000 magnification with a defocus range of 1.5–3.0 μm.

Image processing

Micrographs were checked by optical diffraction and digitized on a Nikon Coolscan 9000 ED with a step size of 10 μm. The digitized images were coarsened by a factor of 3, resulting in a pixel size corresponding to 6 Å at the specimen level. Then images were low-pass-filtered and used to localize particles. Single-molecule images (9030) were extracted semi-automatically from raw micrographs using Boxer (Ludtke et al., 1999) and analysed using IMAGIC V software (van Heel et al., 1996). The phase-contrast-transfer function was corrected by phase flipping. In a first approach, the SAXS envelope was used as a starting model to align apo-Hsp90 particle images using the MRA (multi-reference alignment) program included in IMAGIC V software (van Heel et al., 1996). Images were then grouped into classes and averaged using the MSA (multi-statistical alignment) procedure. From class averages, a three-dimensional model was computed by angular reconstitution using the SAXS model as a reference. Two-dimensional projections were computed from the reconstructed volume and used as new references to align raw images. In a second and independent approach, an analysis without the initial starting three-dimensional model was performed. A total of 900 references were extracted from the low-pass-filtered images of frozen-hydrated apo-Hsp90 and used to align raw apo-Hsp90 particle images. Aligned images were then grouped into classes using the MSA procedure. The best class averages were then used as references to perform a new alignment cycle of apo-Hsp90 particle images. Images were grouped into classes in which most class averages referred to the three-dimensional model previously described. Three views were selected to start the reconstruction process using the angular reconstruction program. The class averages incompatible with this model were analysed separately, and corresponded to the projection of a three-dimensional model of apo-Hsp90 that is more compact than the

main model. Again, three singular views were selected to start the reconstruction process. The two three-dimensional structures of apo-Hsp90 were together iteratively refined in comparing the reprojections of the three-dimensional models with their corresponding class averages. The best results were obtained when applying C2 symmetry, and this is consistent with the dimeric nature of Hsp90 and with previous results obtained by SAXS. The estimated resolution, using an FSC (Fourier shell correlation) coefficient of 0.5 (van Heel et al., 2000), is ~28 Å for the EM map of the fully open state and ~40 Å for the EM map of the semi-open state of apo-Hsp90. Thresholds of all the EM densities were defined to correspond to the volume occupancy of a dimer of Hsp90. Surface representations of apo-Hsp90 were performed using Chimera software (Pettersen et al., 2004).

Acknowledgments

We thank Maria G. Catelli for helpful discussions in the initial phase of this work and the 'Ligue contre le Cancer' for financial support (grant to Maria G. Catelli), David A. Agard for providing the atomic co-ordinates of apo-HtpG and Juliana Berland for critically reading this paper. This work was partly funded by Daresbury's Synchrotron grant number 40116 (to C.G., V.P., P.B., R.M.B. and J.F.D.), by grant BIO2007-61336 from the Ministerio de Educación y Ciencia (to J.F.D.) and by Rennes Métropole (to E.G. and D.T.).

References

Ali, M.M., Roe, S.M., Vaughan, C.K., Meyer, P., Panaretou, B., Piper, P.W., Prodromou, C. and Pearl, L.H. (2006) Crystal structure of an Hsp90–nucleotide–p23/Sba1 closed chaperone complex. Nature **440**, 1013–1017

Andreu, J.M., Diaz, J.F., Gil, R., de Pereda, J.M., Garcia de Lacoba, M., Peyrot, V., Briand, C., Towns-Andrews, E. and Bordas, J. (1994) Solution structure of Taxotere-induced microtubules to 3-nm resolution. The change in protofilament number is linked to the binding of the taxol side chain. J. Biol. Chem. **269**, 31785–31792

Buchner, J. (1999) Hsp90 & Co. – a holding for folding. Trends Biochem. Sci. **24**, 136–141

Chacon, P., Diaz, J.F., Moran, F. and Andreu, J.M. (2000) Reconstruction of protein form with X-ray solution scattering and a genetic algorithm. J. Mol. Biol. **299**, 1289–1302

Csermely, P., Kajtar, J., Hollosi, M., Jalsovszky, G., Holly, S., Kahn, C.R., Gergely, Jr, P., Soti, C., Mihaly, K. and Somogyi, J. (1993) ATP induces a conformational change of the 90-kDa heat shock protein (Hsp90). J. Biol. Chem. **268**, 1901–1907

Csermely, P., Schnaider, T., Soti, C., Prohaszka, Z. and Nardai, G. (1998) The 90-kDa molecular chaperone family: structure, function, and clinical applications. A comprehensive review. Pharmacol. Ther. **79**, 129–168

Diaz, J.F., Andreu, J.M., Diakun, G., Towns-Andrews, E. and Bordas, J. (1996) Structural intermediates in the assembly of taxoid-induced microtubules and GDP-tubulin double rings: time-resolved X-ray scattering. Biophys. J. **70**, 2408–2420

Garnier, C., Barbier, P., Gilli, R., Lopez, C., Peyrot, V. and Briand, C. (1998a) Heat-shock protein 90 (hsp90) binds *in vitro* to tubulin dimer and inhibits microtubule formation. Biochem. Biophys. Res. Commun. **250**, 414–419

Garnier, C., Protasevich, I., Gilli, R., Tsvetkov, P., Lobachov, V., Peyrot, V., Briand, C. and Makarov, A. (1998b) The two-state process of the heat shock protein 90 thermal denaturation: effect of calcium and magnesium. Biochem. Biophys. Res. Commun. **249**, 197–201

Garnier, C., Barbier, P., Devred, F., Rivas, G. and Peyrot, V. (2002) Hydrodynamic properties and quaternary structure of the 90 kDa heat-shock protein: effects of divalent cations. Biochemistry **41**, 11770–11778

Harris, S.F., Shiau, A.K. and Agard, D.A. (2004) The crystal structure of the carboxy-terminal dimerization domain of htpG, the *Escherichia coli* Hsp90, reveals a potential substrate binding site. Structure **12**, 1087–1097

Hawle, P., Siepmann, M., Harst, A., Siderius, M., Reusch, H.P. and Obermann, W.M. (2006) The middle domain of Hsp90 acts as a discriminator between different types of client proteins. Mol. Cell. Biol. **26**, 8385–8395

Koyasu, S., Nishida, E., Kadowaki, T., Matsuzaki, F., Iida, K., Harada, F., Kasuga, M., Sakai, H. and Yahara, I. (1986) Two mammalian heat shock proteins, HSP90 and HSP100, are actin-binding proteins. Proc. Natl. Acad. Sci. U.S.A. **83**, 8054–8058

Kozin, M.B. and Svergun, D.I. (2001) Automated matching of high- and low-resolution structural models. J. Appl. Cryst. **34**, 33–41

Ludtke, S.J., Baldwin, P.R. and Chiu, W. (1999) EMAN: semiautomated software for high-resolution single-particle reconstructions. J. Struct. Biol. **128**, 82–97

Maruya, M., Sameshima, M., Nemoto, T. and Yahara, I. (1999) Monomer arrangement in HSP90 dimer as determined by decoration with N- and C-terminal region specific antibodies. J. Mol. Biol. **285**, 903–907

Meyer, P., Prodromou, C., Hu, B., Vaughan, C., Roe, S.M., Panaretou, B., Piper, P.W. and Pearl, L.H. (2003) Structural and functional analysis of the middle segment of Hsp90: implications for ATP hydrolysis and client protein and cochaperone interactions. Mol. Cell **11**, 647–658

Pearl, L.H. and Prodromou, C. (2006) Structure and mechanism of the hsp90 molecular chaperone machinery. Annu. Rev. Biochem. **75**, 271–294

Pettersen, E.F., Goddard, T.D., Huang, C.C., Couch, G.S., Greenblatt, D.M., Meng, E.C. and Ferrin, T.E. (2004) UCSF Chimera – a visualization system for exploratory research and analysis. J. Comput. Chem. **25**, 1605–1612

Phillips, J.J., Yao, Z.P., Zhang, W., McLaughlin, S., Laue, E.D., Robinson, C.V. and Jackson, S.E. (2007) Conformational dynamics of the molecular chaperone Hsp90 in complexes with a co-chaperone and anticancer drugs. J. Mol. Biol. **372**, 1189–1203

Prodromou, C., Roe, S.M., O'Brien, R., Ladbury, J.E., Piper, P.W. and Pearl, L.H. (1997) Identification and structural characterization of the ATP/ADP-binding site in the Hsp90 molecular chaperone. Cell **90**, 65–75

Prodromou, C., Panaretou, B., Chohan, S., Siligardi, G., O'Brien, R., Ladbury, J.E., Roe, S.M., Piper, P.W. and Pearl, L.H. (2000) The ATPase cycle of Hsp90 drives a molecular 'clamp' via transient dimerization of the N-terminal domains. EMBO J. **19**, 4383–4392

Richter, K. and Buchner, J. (2006) Hsp90: twist and fold. Cell **127**, 251–253

Richter, K., Moser, S., Hagn, F., Friedrich, R., Hainzl, O., Heller, M., Schlee, S., Kessler, H., Reinstein, J. and Buchner, J. (2006) Intrinsic inhibition of the Hsp90 ATPase activity. J. Biol. Chem. **281**, 11301–11311

Shiau, A.K., Harris, S.F., Southworth, D.R. and Agard, D.A. (2006) Structural analysis of *E. coli* Hsp90 reveals dramatic nucleotide-dependent conformational rearrangements. Cell **127**, 329–340

Stebbins, C.E., Russo, A.A., Schneider, C., Rosen, N., Hartl, F.U. and Pavletich, N.P. (1997) Crystal structure of an Hsp90-geldanamycin complex: targeting of a protein chaperone by an antitumor agent. Cell **89**, 239–250

Svergun, D.I. (1992) Determination of the regularization parameter in indirect-transform methods using perceptual criteria. J. Appl. Cryst. **25**, 495–503

Svergun, D.I. (1999) Restoring low resolution structure of biological macromolecules from solution scattering using simulated annealing. Biophys. J. **76**, 2879–2886

van Heel, M., Harauz, G., Orlova, E.V., Schmidt, R. and Schatz, M. (1996) A new generation of the IMAGIC image processing system. J. Struct. Biol. **116**, 17–24

van Heel, M., Gowen, B., Matadeen, R., Orlova, E.V., Finn, R., Pape, T., Cohen, D., Stark, H., Schmidt, R., Schatz, M. et al. (2000) Single-particle electron cryo-microscopy: towards atomic resolution. Q. Rev. Biophys. **33**, 307–369

Vaughan, C.K., Gohlke, U., Sobott, F., Good, V.M., Ali, M.M., Prodromou, C., Robinson, C.V., Saibil, H.R. and Pearl, L.H. (2006) Structure of an Hsp90–Cdc37–Cdk4 complex. Mol. Cell **23**, 697–707

Volkov, V.V. and Svergun, D.I. (2003) Uniqueness of *ab initio* shape determination in small-angle scattering. J. Appl. Cryst. **36**, 860–864

Whitesell, L. and Lindquist, S.L. (2005) HSP90 and the chaperoning of cancer. Nat. Rev. Cancer **5**, 761–772

Yonezawa, N., Nishida, E., Sakai, H., Koyasu, S., Matsuzaki, F., Iida, K. and Yahara, I. (1988) Purification and characterization of the 90-kDa heat-shock protein from mammalian tissues. Eur. J. Biochem. **177**, 1–7

Zhang, W., Hirshberg, M., McLaughlin, S.H., Lazar, G.A., Grossmann, J.G., Nielsen, P.R., Sobott, F., Robinson, C.V., Jackson, S.E. and Laue, E.D. (2004) Biochemical and structural studies of the interaction of Cdc37 with Hsp90. J. Mol. Biol. **340**, 891–907

Received 26 October 2007/18 December 2007; accepted 24 January 2008

Published as Immediate Publication 24 January 2008, doi:10.1042/BC20070149